İPHE

A simulation of charge deposition and collection in silicon microstrip detectors

P. Koppenburg

Institut de Physique des Hautes Energies, Université de Lausanne

Abstract

This note describes the simulation of charge deposition and collection in silicon detectors that has been used to reproduce VELO testbeam resolution measurements.

E-mail: `Patrick.Koppenburg@cern.ch`
`http://www-iphe.unil.ch/~pkoppenb/silsim.html`

Contents

1 Introduction

Very precise resolution measurements have been performed at the 1999 vertex locator (VELO) testbeam [1, 2] that could not be reproduced at a satisfactory level by the standard VELO simulation (implemented in the SICB package). A more detailed simulation based on Ref. [3] and including more physics processes has been developed and agrees with the measurement at the micron level. This note presents the basic underlying theory, the implementation choices and approximations and some results of the simulation.

1.1 Included processes

In the presently used digitization program (SICBDST [4, 5]) the charge deposition is uniformly distributed along the track path and collected by the strips along straight field lines. This *geometrical* model predicts much lower resolution than observed in the laboratory.
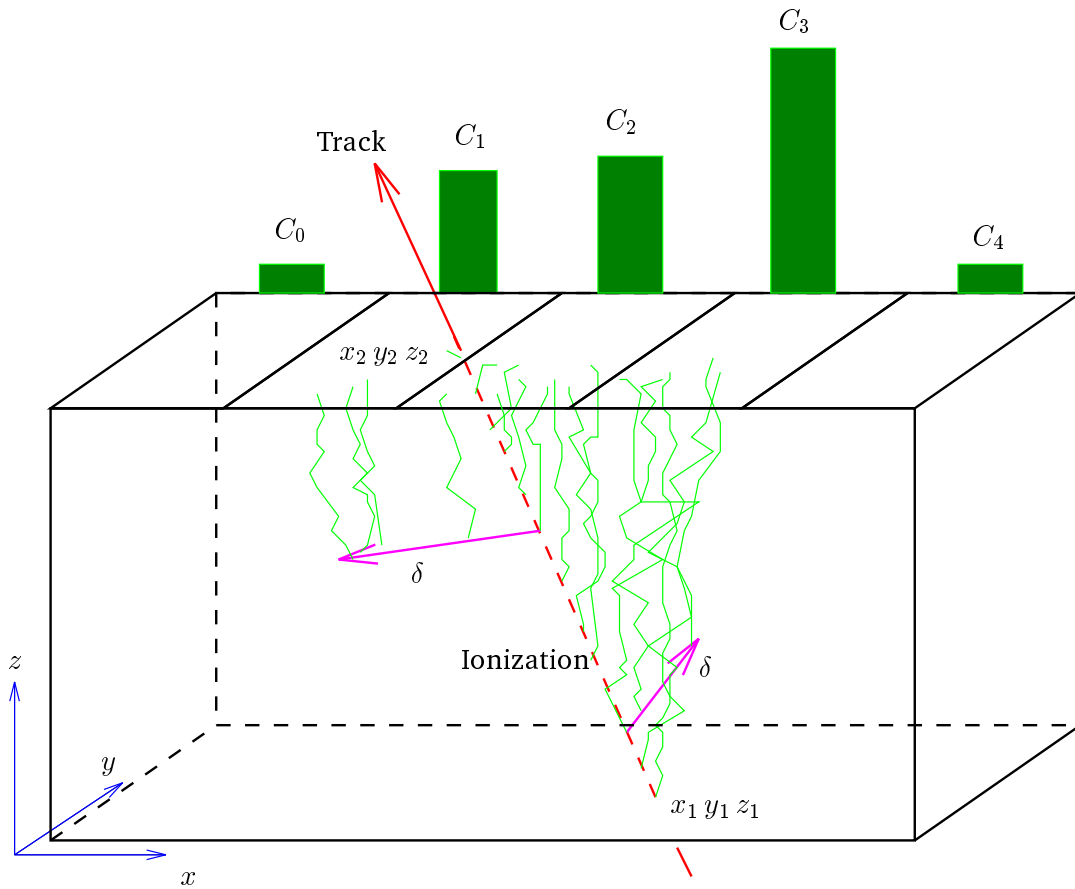
Figure 1: *Charge deposition in silicon. A track enters the silicon in x_1, y_1, z_1 and exits in x_2, y_2, z_2. δ-rays are generated. Charge is deposited along the path of the track and the δ-rays, and drifts towards the strips. The total signal C_i collected on strip i is given by all collected charge carriers and a small fraction of the neighbour strips' charge. Throughout this note we consider that the silicon planes are perpendicular to the z axis and the strips parallel to the y axis.*

The present simulation is considering a local region of interest of a few strips width. The curvature of r-strips is neglected and no boundaries are considered. It is assumed that only one track crosses the considered area, but this is not a limitation as the total charge of several tracks can be added. Figure 1 shows a typical area of silicon traversed by one inclined track emitting two δ-rays. We define the z axis to be perpendicular to the silicon plane (as is the case in the VELO) and the y axis to be (locally) parallel to the strips which consequently measure the x coordinate. The center of the region of interest is x_true, the x position of the track in the middle of the silicon layer ($x_\mathrm{true} = \frac{1}{2}(x_1 + x_2)$ on Figure 1).

The model contains:

- The emission of δ-rays

- Inhomogeneous charge distribution along the track

- Diffusion during charge collection

- Capacitive charge coupling between strips

The simulation uses a few GEANT [6] routines to simulate charge distribution smearing but remains decoupled from the GEANT structures to allow a good control of every subprocess.

To compare the results with measured data, the cluster finder algorithm used at testbeam [1] is applied on the output data.

1.2   Modes of operation

In the simulation of the charge collection process the charge deposited on each strip is computed. This needs as input the strip width and the readout pitch, which is usually only known at digitization level. It is not foreseen to run the program in two steps — the first being the simulation of physics and the second the simulation of the detector response — as too much data would have to be saved between the two operations.

One can choose to run the program at simulation level, instead of GEANT (as was done to simulate the VELO testbeam results) and store the digitized data. Or one can run the simulation at digitization level, using the raw data as input. This is the mode that could be used in the digitization program (for instance in BRUNEL). The two modes of operation are:

The *a priori* mode. This is the standard way of operation of a charge deposition simulation. All effects are simulated independently and added up to get the total deposited energy.

The *a posteriori* mode. In this mode the total deposited energy is used as input and the simulation tries to recover which physics processes have lead to it. This is the mode to be selected when the simulation is used at digitization level (where the physics simulation, for instance the GEANT based SICBMC program, has already generated the energy deposition in a previous run). The present note describes the simulation from this viewpoint as it is less usual.

1.3 Structure of this note

Section 2 reviews the basic theory of charge deposition in matter. In Section 3 we discuss the implementation and the approximations made. Section 4 shows some predictions of the simulation. The default parameters are those of the 1999 VELO testbeam setup but predictions are also shown for various VELO and Inner Tracker geometries in LHCb running conditions.

2 Theoretical overview

2.1 Ionization and δ-rays energies

The total energy loss rate of a charged particle traversing silicon can be written as

$$-\frac{\mathrm{d}E_{\mathrm{tot}}}{\mathrm{d}l} = \frac{\mathrm{d}E_{\mathrm{ion}}}{\mathrm{d}l} + \frac{\mathrm{d}E_{\delta}}{\mathrm{d}l} \tag{1}$$

where E_{ion} is the ionization energy and E_{δ} is the sum of the kinetic energies of all emitted δ-rays. The infinitesimal step $\mathrm{d}l$ is usually expressed in units of $[\mathrm{g\,cm^{-2}}]$ and is related to the physical length $\mathrm{d}r$ by $\mathrm{d}x = \rho\mathrm{d}r$ (the density ρ is given in Table 1).

Atomic number	Z	14
Atomic weight	A	$28.09\ \mathrm{g\,mol^{-1}}$
Mean excitation energy	I	$175\ \mathrm{eV}$
Density	ρ	$2.33\ \mathrm{g/cm^3}$
$4\pi N_A r_e^2 m_e c^2$	K	$0.307\ \mathrm{MeVmol^{-1}\,cm^2}$
Number of δ per $\mathrm{keV^{-1}g}$	F_δ	$76.5\ \mathrm{keVg^{-1}}$
Radiation length	X_0	$21.82\ \mathrm{g\,cm^{-2}}$

Table 1: *Physical constants of silicon.*

The distributions of E_{ion} and E_{δ} depend on an arbitrary energy cutoff T_{cut} that is the minimal energy for a δ-ray to be considered. The restricted energy loss of a relativistic charged particle of mass M much larger than electron mass m_e, four-momentum $(E, \vec{P})$ and $\beta = \frac{P}{E}$, $\gamma = \frac{E}{M}$ is given by [7]

$$\left.\frac{\mathrm{d}E_{\mathrm{ion}}}{\mathrm{d}l}\right|_{T<T_{\mathrm{cut}}} = Kz^2\frac{Z}{A}\frac{1}{\beta^2}\left[\frac{1}{2}\ln\frac{2m_e c^2\beta^2\gamma^2 T_{\mathrm{up}}}{I^2} - \frac{\beta^2}{2}\left(1 + \frac{T_{\mathrm{up}}}{T_{\mathrm{max}}}\right) - \frac{\delta_{\mathrm{dec}}}{2}\right]. \tag{2}$$

The involved physical constants of silicon are given in Table 1. $T_{\mathrm{up}} = \min(T_{\mathrm{cut}}, T_{\mathrm{max}})$ and

$$T_{\mathrm{max}} = \frac{2m_e c^2\beta^2\gamma^2}{1 + 2\gamma\frac{m_e}{M} + \left(\frac{m_e}{M}\right)^2} \tag{3}$$

is the maximal energy that can be transferred to a free electron. At high energies T_{max} can be expanded in factors of γ^{-1}

$$T_{\mathrm{max}} = E\left[1 - \frac{1}{2\gamma}\left(\frac{M}{m_e} + \frac{m_e}{M}\right) + \mathcal{O}\left(\frac{1}{\gamma^2}\right)\right], \tag{4}$$

3

which can be huge compared to typical δ-ray energies and usually $T_{up} = T_{max}$. Figure 2 shows T_{max} versus the particle's momentum for the most common particles.

The density effect correction δ_{dec} is only important at very high energies. It expresses the fact that the medium is polarised by the particle, which limits the field extension (proportional to $\ln \beta\gamma$) at high energies. We use Sternheimer's parameterization of this effect [8].

2.2 Emission of δ-rays

The kinetic energy distribution of δ-rays for an incoming particle of speed βc and energy E is [7]

$$\frac{\mathrm{d}^2 N_\delta}{\mathrm{d}T_\delta \mathrm{d}l} = \underbrace{\frac{1}{2} K z^2 \frac{Z}{A}}_{F_\delta} \frac{1}{\beta^2} \frac{F(T_\delta)}{T_\delta^2} \tag{5}$$

with [9]

$$F(T_\delta) = \begin{cases} 1 - \frac{\beta^2 T_\delta}{T_{max}} & \text{for spin-0 particles,} \\ 1 - \frac{\beta^2 T_\delta}{T_{max}} + \frac{T_\delta^2}{2E^2} & \text{for spin-}\frac{1}{2} \text{ particles.} \end{cases} \tag{6}$$

An expression for spin-1 particles can also be found in Ref. [9] but is unlikely to be needed. As T_{max} and E are usually much bigger than T_δ, the density (5) is approximately proportional to T_δ^{-2}. Equation (5) can be integrated to get the average number of δ-rays for a
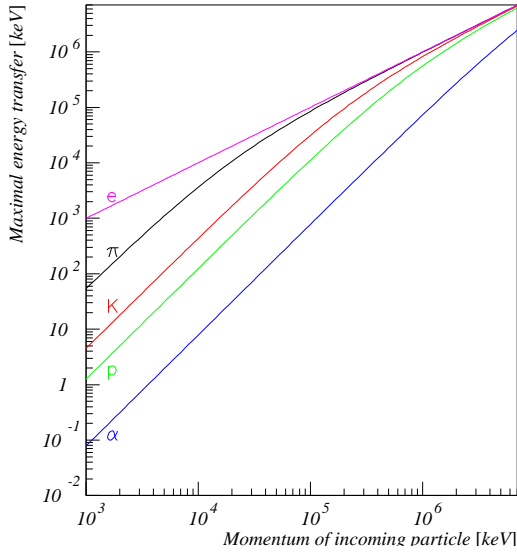
Figure 2: *Maximal energy transfer T_{max} to a free electron versus momentum of an incoming for electron, pion, kaon, proton or α (see equation (3)).*

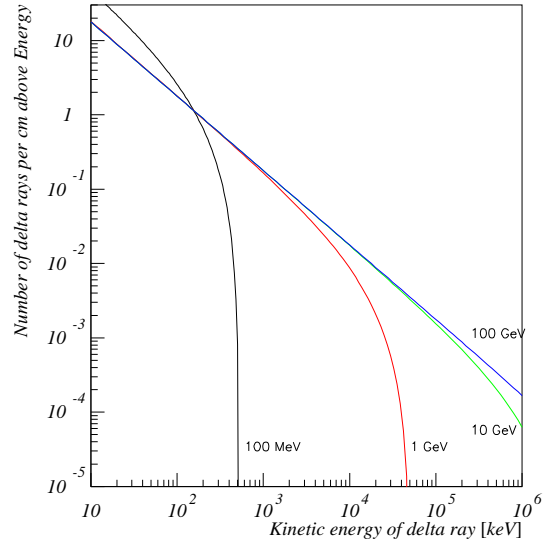Figure 3: *Number of δ-rays per cm above energy T_{cut} versus T_{cut} for incoming pions of $P = 100 \,\mathrm{keV}$ to $1 \,\mathrm{GeV}$ (see equation (7)). At high energies the curve follows $1/T_{cut}$. At lower energies it falls off at $T_{cut} = T_{max}$.*

4

path of length L

$$
\begin{aligned}
\langle n_\delta \rangle &= \int\limits_0^{\rho L} \mathrm{d}l \int\limits_{T_{\mathrm{cut}}}^{T_{\max}} \mathrm{d}T_\delta \frac{F_\delta}{\beta^2} \frac{1 - \frac{\beta^2 T_\delta}{T_{\max}}}{T_\delta{}^2} \\
&= \frac{\rho L F_\delta}{\beta^2} \left[\frac{1}{T_{\mathrm{cut}}} - \frac{1}{T_{\max}} \left(1 + \beta^2 \log \frac{T_{\max}}{T_{\mathrm{cut}}} \right) \right] .
\end{aligned} \tag{7}
$$

Figure 3 shows the number of δ-rays per cm above energy T_{cut} for incoming pions of various energies. For particles above $1\,\mathrm{GeV}$ the $T_{\max}$ correction is negligible and (7) becomes

$$
\langle n_\delta \rangle \approx \frac{\rho L F_\delta}{T_{\mathrm{cut}}}
$$

Reasonable energy cuts T_{cut} are in the range 10–100 keV, depending on the resolution of the detector. We use $T_{\mathrm{cut}} = 20\,\mathrm{keV}$ as default. A high energy particle emits on average one δ-ray with energy $T_\delta > T_{\mathrm{cut}} = 20\,\mathrm{keV}$ per millimeter of silicon.

The total energy E_δ lost to δ-rays is

$$
\frac{\mathrm{d}E_\delta}{\mathrm{d}l} = \int\limits_{T_{\mathrm{up}}}^{T_{\max}} \frac{\mathrm{d}^2 N}{\mathrm{d}T_\delta \mathrm{d}l} T_\delta \mathrm{d}T_\delta = \frac{F_\delta}{\beta^2} \left[\ln \frac{T_{\max}}{T_{\mathrm{up}}} - \beta^2 \left(1 - \frac{T_{\mathrm{up}}}{T_{\max}} \right) \right] . \tag{8}
$$

Adding up equations (2) and (8) and respecting the sign convention defined in (1) one recovers the well known Bethe-Bloch formula [10]

$$
-\frac{\mathrm{d}E_{\mathrm{tot}}}{\mathrm{d}l} = K z^2 \frac{Z}{A} \frac{1}{\beta^2} \left[\frac{1}{2} \ln \frac{2 m_e c^2 \beta^2 \gamma^2 T_{\max}}{I^2} - \beta^2 - \frac{\delta_{\mathrm{dec}}}{2} \right] . \tag{9}
$$

The evolution of E_{tot}, E_{ion} and E_δ with the momentum of the incoming particle is shown in Figure 4.

For thin silicon layers the total lost energy E_{tot} is about Landau distributed (with a larger width because in silicon electrons are bound rather than free as assumed by the Landau theory [11, 12]). For thicker layers the energy loss cannot be neglected compared to the particle's energy and the Vavilov [13] description has to be used. At low energies the Bethe-Bloch equation has to be corrected with some experimental factors [7]. In the scope of this simulation we use the data from [14] shown in Figures 5 and 6 to predict the stopping power.

The recoil angle θ of the δ-ray depends only on the energy E of the incoming particle and the kinetic energy T_δ [15]

$$
\theta = \mathrm{acos} \left(\frac{E + m_e c^2}{\sqrt{E^2 - M^2 c^4}} \sqrt{\frac{T_\delta}{T_\delta + 2 m_e c^2}} \right) . \tag{10}
$$

The distribution of this angle versus T_δ is shown in Figure 7. The more probable low-energy δ-rays are emitted almost perpendicularly to the track.

The range of a low-energy electron in silicon is shown in Figure 8. Electrons of few hundred keV can travel more than $100\,\mu\mathrm{m}$ in silicon and thus affect the resolution.
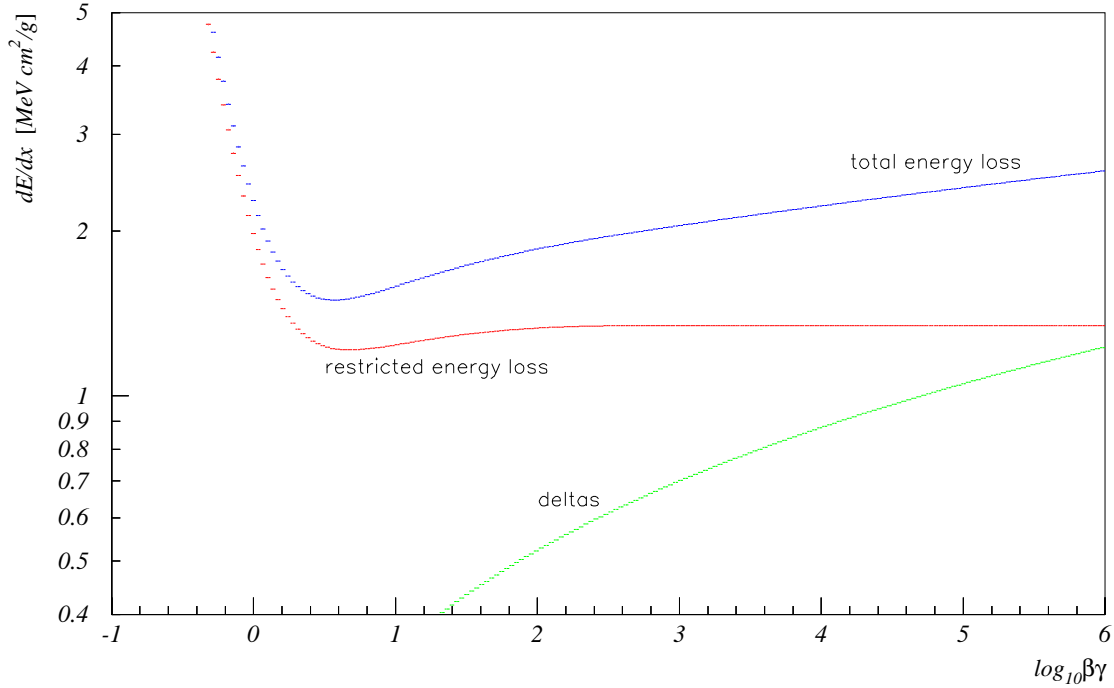
Figure 4: *Stopping power of silicon for pions versus* $\log_{10} \beta\gamma$. *The three curves show the total energy loss (9), the restricted energy loss (2) and their difference corresponding to the energy imparted to δ-rays. A cut $T_{\mathrm{cut}} = 20\,\mathrm{keV}$ is applied.*
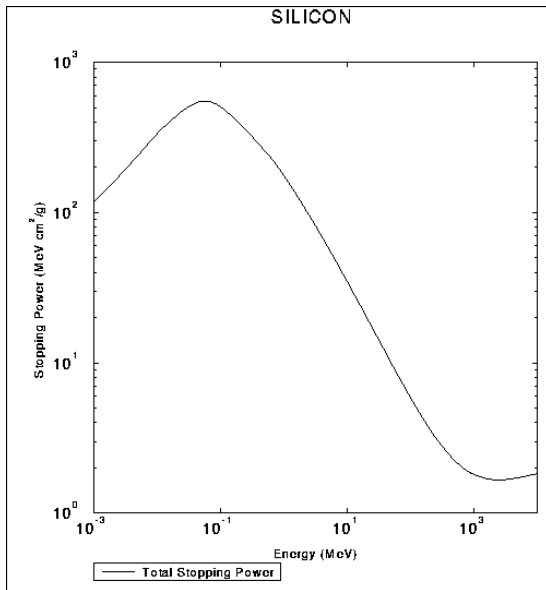

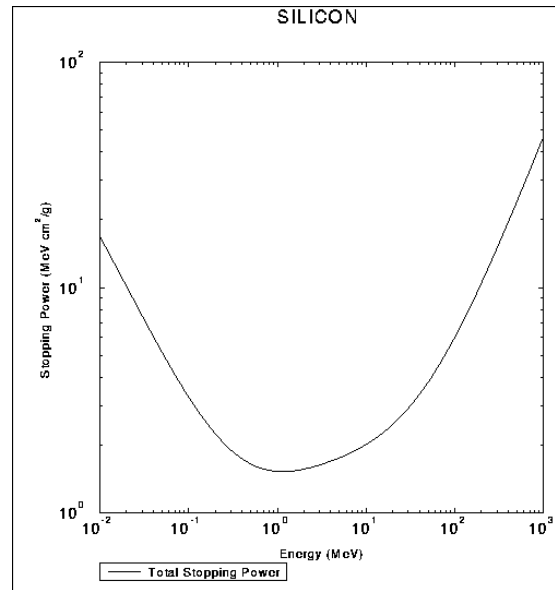Figure 5: Stopping power of protons in silicon. Data from [14].

Figure 6: Stopping power of electrons in silicon. Data from [14].

2.3 Effect of δ-rays on resolution

The emission of δ-rays affects the reconstructed position in two ways

6
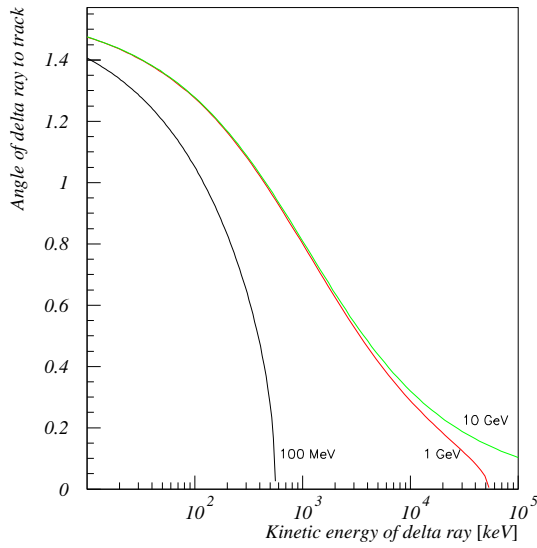
Figure 7: Angle of δ-ray to track versus T_δ for incoming pions of $P \geq 100\,\text{MeV}$. The more probable low-energetic δ-rays are emitted almost perpendicularly to the track.
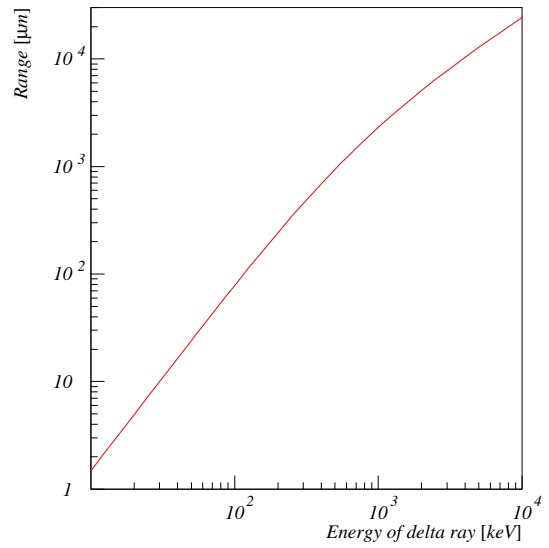
Figure 8: Range of δ-rays in silicon versus energy in the continuous-slowing-down approximation. Data from Ref. [14].
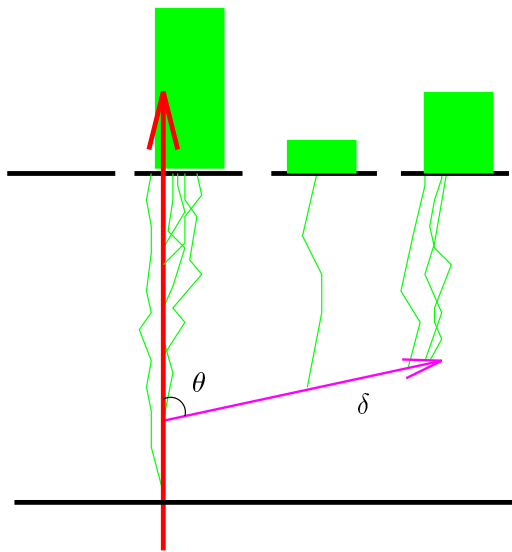
Figure 9: Resolution degradation due to a long range δ-ray.
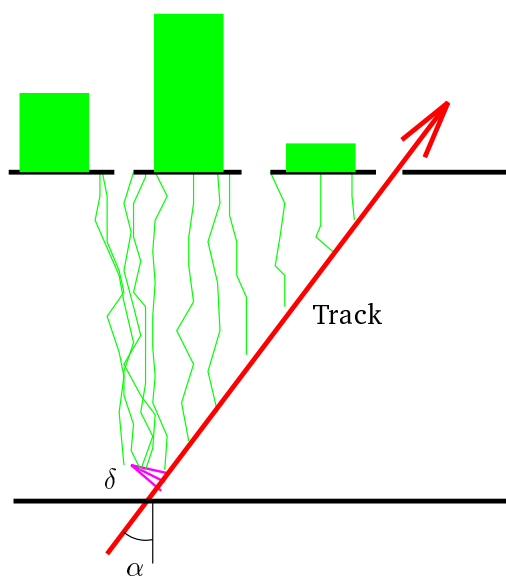
Figure 10: Resolution degradation due to charge deposition inhomogeneity.

Shift due to long range δ-rays Long range δ-rays can artificially enlarge the cluster size. Approximating the energy deposition along the δ-ray path of length R_δ by a uniform distribution and considering an incoming track that is perpendicular to the silicon

plane we can estimate the shift in the reconstructed position

$$\Delta(T_\delta) \approx \frac{\frac{1}{2}T_\delta R_\delta \sin\theta}{T_\delta + E_{\text{ion}}} \tag{11}$$

where we added a correction due to the δ's angle θ (given by equation (10)) compared to the estimate suggested in Ref. [11].

This situation is illustrated in Figure 9. One can estimate contribution of δ-rays of energy T_δ to the overall resolution by multiplying the resolution shift $\Delta(T_\delta)$ by the probability $\frac{\mathrm{d}^2 N}{\mathrm{d}T_\delta \mathrm{d}l}$. Figure 11 shows that δ-rays around 100 keV contribute most to the resolution smearing[1]. This effect affects more perpendicular tracks than inclined tracks.

Shift due to inhomogeneous charge distribution For inclined tracks, the effect on resolution is dominated by the charge deposition inhomogeneity due to the δ-ray.

The most probable energy deposition in a 300 μm thick detector is about $E_{\text{ion}} = 80$ keV. The emission of a $T_\delta = 20$ keV δ-ray traveling only a few microns and starting at one end of the track increases the deposited charge around this location and shifts the cluster center accordingly. This is illustrated in Figure 10. Neglecting the range of the δ-ray, the resulting shift can be estimated by

$$\Delta(T_\delta) \approx \frac{E_\delta}{E_{\text{ion}}} \frac{|\Delta z_\delta|}{\frac{1}{2}\Theta} \sin\alpha \tag{12}$$

where Δz_δ is the vertical distance from the emission point of the δ-ray to the center of the silicon layer, Θ is the thickness and α is the angle of the track.

2.3.1 Tracking and charge deposition of δ-rays

The behaviour of low energy particles is very difficult to predict. GEANT uses the common Molière [16, 17] description of multiple scattering. This model assumes

1. that the angular deflections in single collisions are small,

2. that the medium is homogeneous on the path length l.

Within these limitations the width of the (about Gaussian) angular deflection projected on a plane is [7]

$$\theta_0 = \frac{13.6\,\text{MeV}}{\beta cp} z \sqrt{\frac{l}{X_0}} \left[1 + 0.038 \ln\frac{l}{X_0}\right] = \frac{1}{\sqrt{2}}\theta_0^{\text{space}}.$$

For silicon this becomes

$$\theta_0 \approx \frac{45}{\beta pc\,[\text{keV}]} \sqrt{l\,[\mu\text{m}]} \left[0.57 + 0.038 \ln\left(x\,[\mu\text{m}]\right)\right].$$

Figure 12 shows this angle versus the energy and the path length l. For energies below 100 keV both assumptions cannot be fulfilled simultaneously. A 20 keV electron for instance is deflected by 0.1 rad in 1 Å, which is less than the size of an atom.

---

[1]Note that when the δ-range is much bigger than the strip-pitch it becomes likely that two clusters are formed, one located at the incoming track's position and the other around the end of the δ path.
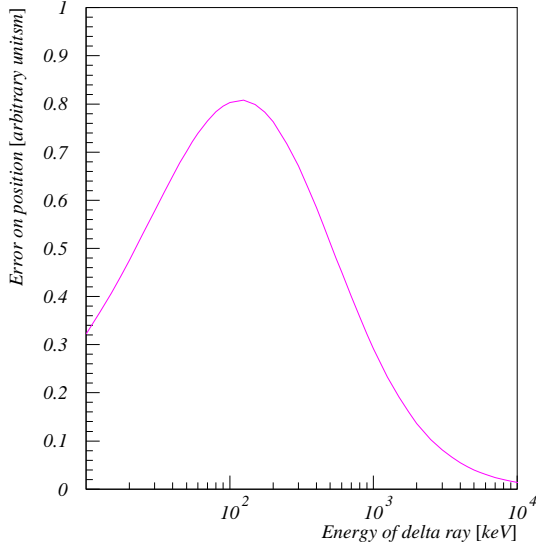
Figure 11: *Weighted resolution degradation $\Delta(T_\delta)\frac{dN}{dT_\delta}$ in arbitrary units versus T_δ for a perpendicular minimum ionising particle.*
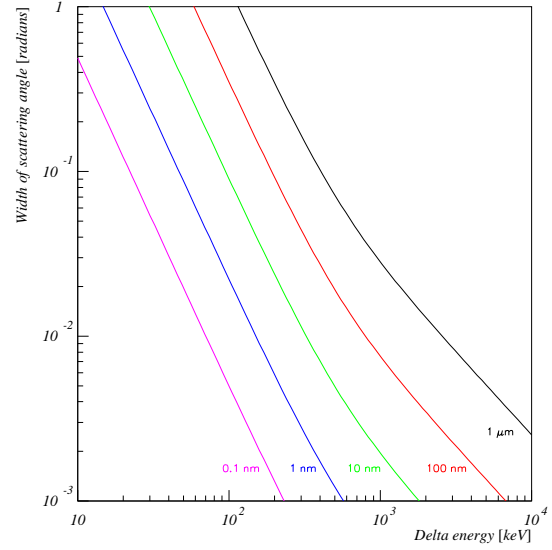

Figure 12: *Width of scattering angle versus energy for various path lengths.*

2.4 Diffusion of primary ionization charge

In an n-type silicon detector with p-type strips (p-on-n) the holes drift to the strips and the electrons to the backplane. In an n-on-n detector, the collected charge carriers are electrons.

The average drift velocity $\vec{v}_i$ ($i = $ e, h) is proportional to the electric field $\vec{E}$ (parallel to the z axis)

$$\vec{v}_i = \mu_i \vec{E} \tag{13}$$

The mobility μ_i is strictly speaking depending on doping concentration. For concentrations below 10^{16} donors/cm^3 the mobilities of electrons and holes are given in Table 2. The total charge collection time $t = \frac{z^2}{V \mu_h}$ is dominated by the collection of the charge carriers created near the backplane. The visible charge on a strip is the integral over the shaping time of

Thickness	Θ	300 μm
Biasing Voltage	V	100 V
Electric field	E	3300 V cm^{-1}
Mobility of holes	μ_{h}	450 cm^2/Vs
Mobility of electrons	μ_{e}	-1400 cm^2/Vs
Collection time of holes	t_{h}	20 ns
Collection time of electrons	t_{e}	7 ns
Temperature	kT	0.025 eV
Lateral diffusion of holes	$\sigma_{\mathrm{h}}(\Theta)$	7 μm
Lateral diffusion of electrons	$\sigma_{\mathrm{e}}(\Theta)$	7 μm

Table 2: *Typical numerical values of some parameters.*

9

the collected current given by Ramo's theorem [18]. When this shaping time is larger than the drift time, only the charge carriers reaching the considered strip contribute to the signal.

The charge collection is affected by the lateral diffusion of the charge carriers which follows a Gaussian distribution of width $\sigma(\Delta z) = \sqrt{2Dt_j(\Delta z)}$. The diffusion coefficient D is

$$D = \frac{kT}{q}\mu_i$$

and $t_j(\Delta z)$ is the time of the drift on a distance Δz. Hence the diffusion width for a charge carrier created at distance Δz from the strip is

$$\sigma_x(\Delta z) = \sqrt{2\frac{kT}{q}\frac{\Theta\Delta z}{V}}. \tag{14}$$

2.5   Charge sharing between strips

In silicon microstrip detectors the capacitive (or sometimes resistive [19]) coupling of neighbouring strips causes a charge sharing between them. Even when the whole charge drifts to a single strip, a small fraction of the signal may be seen on the neighbouring strip. When the main cause for charge sharing is the capacitive coupling between strips, the value of this fraction only depends on the inter-strip and strip-to-backplane capacitances. For a detailed prediction of the charge sharing a simulation of the electronic structure of the silicon detector may be helpful. In the frame of this local model we assume that the charge sharing fraction f is constant over the whole detector. The signal S_i collected on strip i is

$$S_i = \epsilon_i\left[(1-2f)C_i + f\left(C_{i-1} + C_{i+1}\right)\right] \tag{15}$$

where C_i is the charge deposited on strip i and ϵ_i the charge collection efficiency in this strip. We assume that $\epsilon_i \simeq 1$ and hence from (15)

$$\sum_{\mathrm{detector}} S_i = \sum_{\mathrm{detector}} C_i.$$

In Ref. [1] the fraction f has been measured considering high-energy tracks passing in-between two strips. The results are

$$f = \begin{cases} (5.3 \pm 0.3)\% & \text{for } 40\,\mu\text{m strip pitch} \\ (4.7 \pm 0.2)\% & \text{for } 60\,\mu\text{m strip pitch} \end{cases}$$

These small values are typical for detectors where all strips are read out. Bigger charge sharing fractions around 30% arise in detectors with floating strips.

3   Implementation

As this simulation includes a description of the strip geometry it must be called in the same run as the digitization.

3.1 Ionization and δ-ray energies

The ionization energy E_{ion} is sampled using GLANDZ [6]. This routine uses equation (2) and adds some fluctuations.

The production of δ-rays depends on the mode of operation.

A priori mode: The number of δ-rays N_δ is sampled using a Poisson distribution of mean $\langle n_\delta \rangle$ (equation (7)). The energy of each δ-ray is generated using the method described in Section 3.1.1.

A posteriori mode: The simulation uses the already simulated entry and exit points of the track and the deposited energy E_{tot} and tries to recover what has happened in the detector. The total energy of all δ rays is estimated as:

$$E_\delta = E_{\text{tot}} - E_{\text{ion}}.$$

When E_δ is smaller than the energy cutoff T_{cut}, no δ-rays are produced and the ionization energy is reset to $E_{\text{ion}} = E_{\text{tot}}$. The number of δ-rays is found using Bayes' theorem as explained in Section 3.1.2.

3.1.1 Generation of the δ-ray's energy

The generation of the energy distributed as (5) is done using the variable change

$$u_\delta = \frac{1}{T_\delta}. \tag{16}$$

Equation (5) transforms to

$$\frac{\mathrm{d}N_\delta}{\mathrm{d}u_\delta} = \frac{\mathrm{d}N_\delta}{\mathrm{d}T_\delta} \left| \frac{\mathrm{d}T_\delta}{\mathrm{d}u_\delta} \right| = L\rho F_\delta \frac{1}{\beta^2} F(1/u_\delta) \tag{17}$$

with

$$\frac{1}{T_{\text{cut}}} = u_{\text{cut}} \geq u_\delta > u_{\text{max}} = \frac{1}{T_{\text{max}}}$$

and $F(T_\delta)$ is defined in (6). The distribution is generated using the throw-awaymethod. Two uniform-distributed random numbers r_1 and r_2 ($0 \leq r_i \leq 1$, $i = 1, 2$) are generated and the value

$$u_\delta = r_1 u_{\text{cut}}$$

is calculated. The inverse kinetic energy u_δ is accepted if $F(1/u_\delta) \leq r_2$. The efficiency of this trial is close to 100% as usually $u_{\text{max}} \ll u_{\text{cut}}$.

3.1.2 Generation of the number of δ-rays

The probability $\mathcal{P}\left(N_\delta = n \,\middle|\, \sum_{N_\delta} T_\delta = E_\delta\right)$ of emitting n δ-rays knowing their total energy E_δ is shown in Figure 13. The probability of emitting more than one δ-ray remains small even when the total energy of all δ-rays is large.

In the simulation of testbeam results [1] a naive procedure, generating δ-rays according to distribution (5) until the available total energy E_δ is reached was used. This leads
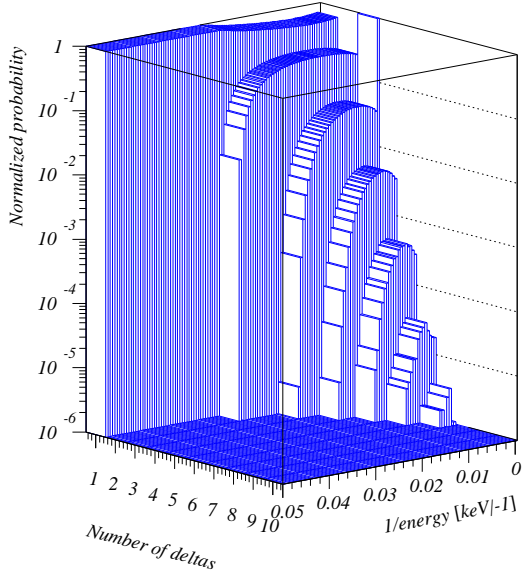
Figure 13: *Probability of N_δ δ-rays knowing the total energy E_δ (Equation (18)) versus the inverse total energy $1/E_\delta$ for $T_{\text{cut}} = 20\,\text{keV}$ and $\langle n_\delta \rangle = 0.3$.*
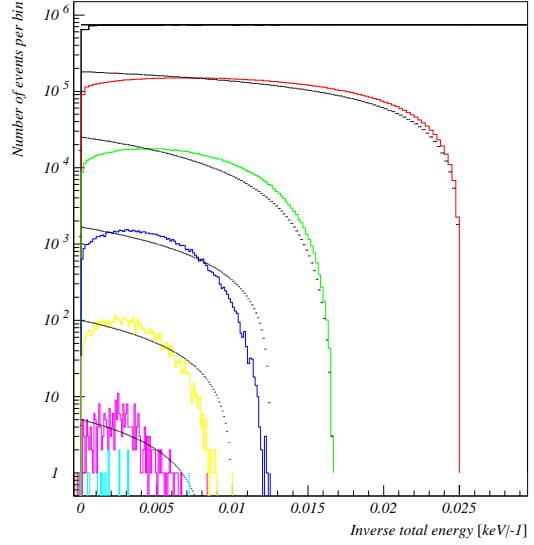
Figure 14: *Number of δ-rays N_δ versus total inverse energy $1/E_\delta$ for $T_{\text{cut}} = 20\,\text{keV}$ and $\langle n_\delta \rangle = 0.3$. The a posteriori approximation functions are superimposed on the histograms obtained with the a priori simulation.*

to a huge number of δ-rays for high total energies and hence over-estimates the resolution smearing for tracks depositing a very high energy in the silicon. A more reliable approach is described below.

It is possible to compute the energy probability density for any given number of δ-rays and then to recover the probability distribution of N_δ at fixed total energy using Bayes' theorem. d Knowing the total energy $\sum_{N_\delta} T_\delta = E_\delta$ of all emitted δ-rays one generates the number of δ-rays using the probabilities

$$\mathcal{P}\left(N_\delta = n \,\middle|\, \sum_{N_\delta} T_\delta = E_\delta\right) = \mathcal{P}\left(N_\delta = n\right) f_n(1/E_\delta). \tag{18}$$

The functions f_n, their derivation and the approximations made are given in Appendix A. They are defined in the range $0 < \frac{1}{E_\delta} \leq \frac{n}{T_{\text{cut}}}$ and normalized on that range. The probabilities $\mathcal{P}\left(N_\delta = n\right)$ are given by a Poissonian distribution of mean $\langle n_\delta \rangle$ that is given by (7).

Figure 14 compares the distributions of the total energy E_δ for various number of δ-rays in the a priori and a posteriori modes using equation (18).

Using the probabilities $\mathcal{P}\left(N_\delta = n | \sum_{N_\delta} T_\delta = E_\delta\right)$ the generation of N_δ is straightforward. The kinetic energies of the $N_\delta - 1$ first δ-rays are generated according to the procedure explained in Section 3.1.1 while the energy of the last δ-ray is fixed in order to reach the total energy E_δ. If this energy is not between T_{cut} and T_{max} the energies of the previous δ-rays are generated again. This causes a negligible bias on the δ-ray energy distribution.

The initial position and azimuthal angles with respect to the track of the δ-ray are uniformly distributed.

3.2 Tracking and primary ionization

The incoming track and the δ-rays are tracked in small steps ($\mathcal{O}\left(1\,\mu\mathrm{m}\right)$) along their path in the silicon. No multiple scattering is applied to the incoming track as it is negligible inside the silicon layer. Molière scattering is applied to δ-rays with energy above $T_{\mathrm{scat}} = \mathcal{O}\left(100\,\mathrm{keV}\right)$. At lower energies, a probability that the δ-ray stops in each step depending on its kinetic energy is calculated using the experimental model describing the attenuation of electrons in matter as $\sqrt[4]{N} \propto L$, where N is the number of electrons that reach a depth L.

The energy lost by the particles in each segment is sampled using the GEANT routine GLANDZ. For the incoming particle the ionization energy deposited in each segment is renormalised in order to sum up to the total ionization energy E_{ion}.

3.3 Diffusion

The energy deposited in each segment is converted into electron-hole pairs and the charge carriers are collected into the strips following the (straight) field lines adding some horizontal diffusion. The fraction of the charge collected in each strip is

$$f_i = \frac{1}{\sqrt{2\pi}} \int\limits_{x_i - x_s - p/2}^{x_i - x_s + p/2} e^{-\frac{x^2}{2\sigma_x^2}}\,\mathrm{d}x. \tag{19}$$

where x_i and p are the center position and the pitch of strip i, and $\left(x_s, y_s, z_s\right)$ is the middle position of the segment. The diffusion width σ_x defined in equation (14) depends on the drift distance $z - z_s$.

This procedure improves the simulation described in References [3, 19] by spreading the charge over all strips rather than assigning the total charge of a segment to one single strip. Yet this model is not strip-length independent since all the charge of a segment is put onto its center before diffusion. This is reasonable only for segments that are much smaller than the resolution of the detector.

3.4 Charge sharing

The total charge collected by each strip is obtained as sum of the contributions of all segments of the track and the δ-rays. The charge is shared with the neighbouring strips following equation (15).

4 Simulation results

The present simulation was developed in order to reproduce the testbeam results. The parameters of the simulation are given in Table 3. In Section 4.1 we present the predictions of the simulation using these settings and confront them with experimental values. Section 4.2 describes the effects which contribute to the resolution: diffusion, δ-rays and charge sharing. In Section 4.3 we describe an algorithm which corrects the position determination from finite strip dimension effects. Section 4.4 and 4.6 show the expected resolutions and cluster sizes with the preferred VELO and Inner Tracker geometries and settings at LHCb.

| Parameter | | VELO | | | Inner |
		Testbeam	Optimized	TDR	Tracker
Type		p-on-n	n-on-n	n-on-n	n-on-n
Thickness	z	300 μm	220 μm	300 μm	300 μm
Pitch (r)	p	40-100 μm	20-40 μm	40-60 μm	235 μm
Charge sharing fraction	f	4.7-5.3 %	5.0 %	5.0 %	5.0 %
Biasing Voltage	V	80 V	40 V	70 V	100 V
Temperature	kT	0.025 eV	0.025 eV	0.025 eV	0.025 eV
Signal to noise ratio	S/N	50	15	20	20
Threshold	C	15	5	5	5
Incoming particle		μ^+	π^+	π^+	π^+
Particle's Energy	E	120 GeV	1-100 GeV	1-100 GeV	1-100 GeV

Table 3: *Default values used in the simulation. Three* VELO *geometries are considered: The testbeam geometry as used in the 1999 testbeam run [1], the optimized* VELO *geometry [20] and the TDR baseline solution [21]. The Silicon Inner Tracker geometry is described in Ref. [22].*

4.1   Resolution with VELO testbeam settings

In this section we present the predictions of the simulation using the settings and detector geometry of the autumn 1999 VELO testbeam run given in Table 3. We compare the resolution measured in the laboratory with the prediction of the simulation.

The same cluster finder algorithm is used in both cases. It is described in Ref. [1]. It essentially looks for strips with a very high signal compared to the measured noise and checks for neighbours with a high signal. A cluster can contain up to 5 strips.

At testbeam, the word "resolution" refers to the width of the distribution of the extrapolated position of a track and the closest weighted cluster center. The contribution of multiple scattering and alignment to the resolution is estimated to be about 1 μm. It has to be added in quadrature with the contribution from the detector — 5 to 30 μm— and can hence be neglected.

In the simulation we call "resolution" the rms of the $x_{\rm CM} - x_{\rm true}$ distribution where $x_{\rm CM}$ is the weighted center of the cluster and $x_{\rm true}$ the Monte Carlo true position of the track in the center of the silicon layer. Such a distribution is shown in Figure 21. The same clustering algorithm as at testbeam is used in the simulation. It is described in Ref [1].

The relevant angle for the study of inclined tracks is the projected angle of the track in the x–z plane (see Figure 1). This angle is called *projected angle* in Ref. [1] and simply *angle* in this note. In the figures we plot the variables of interest versus the *slope* as the behaviour of charge collection depends on this variable. As the angles are small, the distinction is not of great importance.

The track angle distribution covers the range from 0 to 240 mrad but is peaked at some values around 20, 80, 120 and 200 mrad. In the simulation a flat angle distribution was used for all plots. Thus only angle-independent variables or distributions of variables versus angle can be used to compare the simulation with the experimental values. All distributions that are integrated over the whole slope range cannot be directly compared [2].

The simulation of charge deposition does not contain a description of electronic noise.

---

[2]Except for the Landau distribution that depends on the slope very weakly and where a good agreement was found.
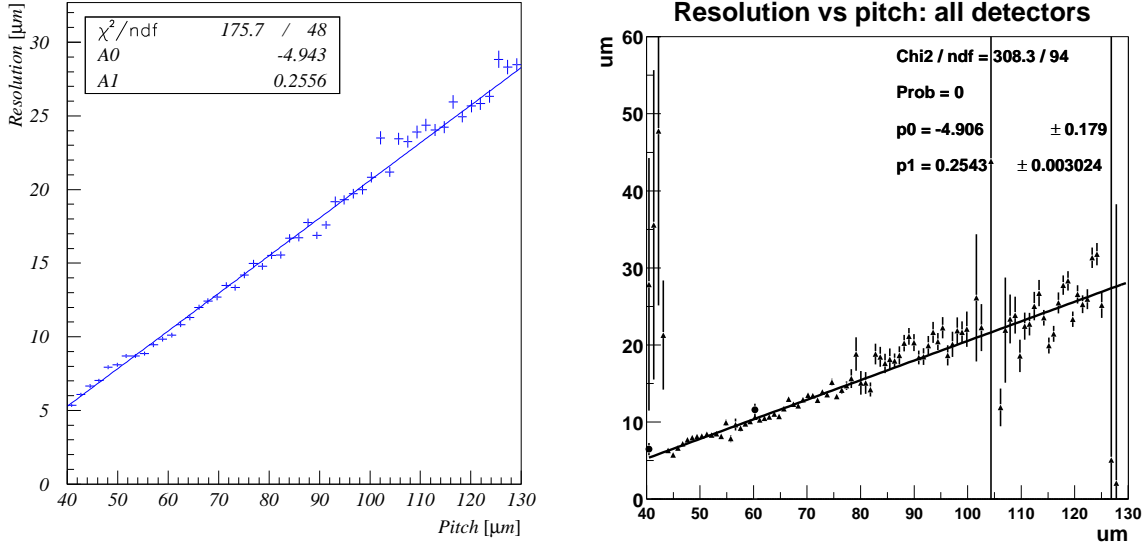
Figure 15: Resolution of perpendicular tracks versus pitch in the VELO testbeam conditions (left side). A linear fit is performed. The experimental data taken from [2] is shown on the right side for comparison. The curves agree within statistical errors.

We have added a Gaussian noise to every strip such that the most probable signal to noise ratio is $S/N = 50$ as measured in testbeam. See [23] for a detailed description of the noise in the detectors used in the 1999 testbeam.

4.1.1 Resolution of perpendicular tracks versus pitch

At the autumn 1999 testbeam the resolution for perpendicular tracks at various strip pitches has been measured [2]. This analysis has been performed using mainly φ-detectors. Figure 15 shows the simulated and measured data. A linear behaviour of the resolution versus the pitch is observed in the range of tested pitches. The equations of the linear fits are:

$$\text{resolution} = (0.2543 \pm 0.0030) \cdot \text{pitch} - (4.906 \pm 0.179) \qquad \text{(Testbeam)} \qquad (20)$$
$$\text{resolution} = (0.2556 \pm 0.0014) \cdot \text{pitch} - (4.943 \pm 0.094) \qquad \text{(Simulation)}. \qquad (21)$$

They agree within errors.

The two measurements of the resolution using r-detectors at pitches of 40 and 60 μm are about one micron above the measurement using the φ-detectors. There seems to be a better resolution in φ than in r. This is not yet understood.

4.1.2 Cluster size and resolution versus slope

One of the distributions of interest is the distribution of cluster sizes versus the slope. This is very sensitive to diffusion and charge sharing. The simulated and measured distributions are shown in Figure 16. They agree within errors.

The agreement of the resolution versus the slope is less striking. The simulated curves shown in Figure 17 underestimate the resolution by about 1 μm both for 40 μm and 60
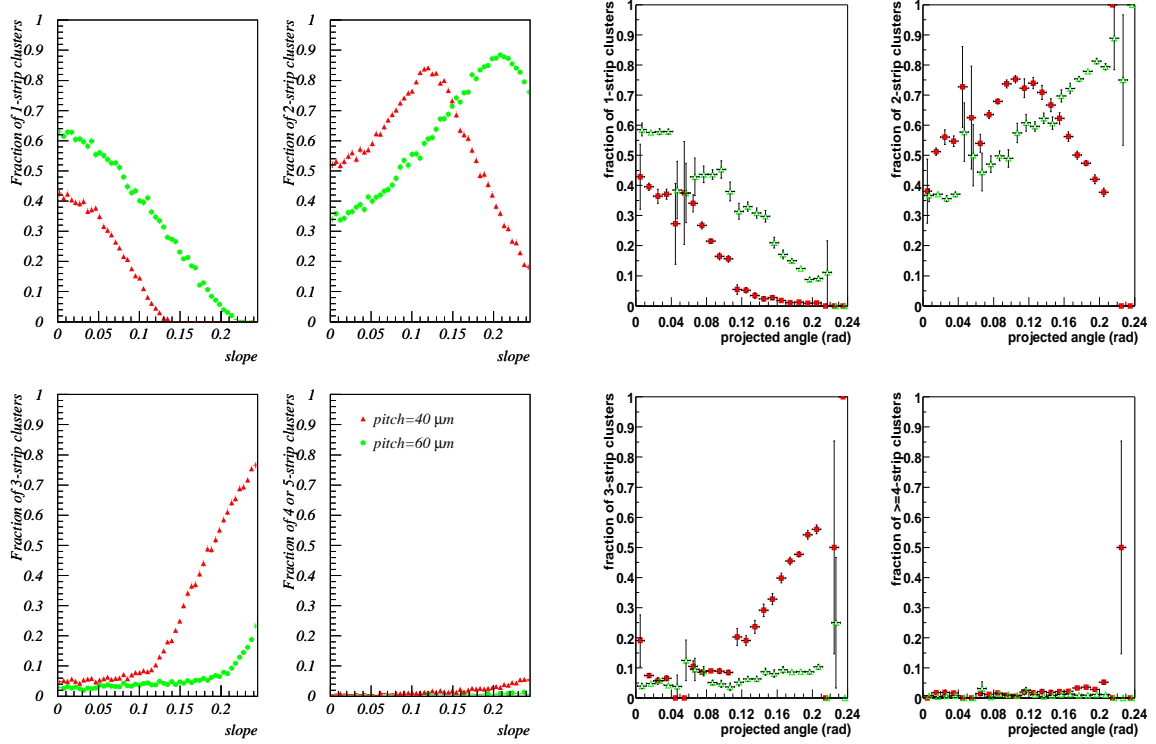
15

Figure 16: Fractions of 1, 2, 3 and 4 or 5 strip clusters versus slope for 40 and 60 μm strip pitches in VELO testbeam conditions. Left: simulation. Right: Measured data taken from [1].

μm strip pitches. This difference is compatible with the observed r-φ discrepancy (see Section 4.1.1).

4.2 Effect of diffusion, charge sharing and δ-rays

Figure 18 shows the contribution of diffusion, charge sharing and δ-rays to the resolution versus slope. The curve obtained with all effects switched off starts at a resolution of about pitch/$\sqrt{12}$ for perpendicular tracks and decreases with increasing slope. A minimum is reached at slope = pitch/thickness = 0.13. This behaviour is about what is coded in the present digitization scheme (used in SICBDST).

4.2.1 Diffusion

When diffusion is added the resolution becomes much better for low angle tracks and then tends towards the previous curve. The reason for this improvement is the lower number of 1-strip clusters, which contain little information about the position of the track. In the range of usable voltages ($\mathcal{O}\,(100)$ V) the resolution becomes better at lower voltages.

4.2.2 δ-rays

The presence of δ-rays hardly affects the resolution of low-angle tracks. The effect is more pronounced for high angle tracks and reaches about two microns. This case reflects the
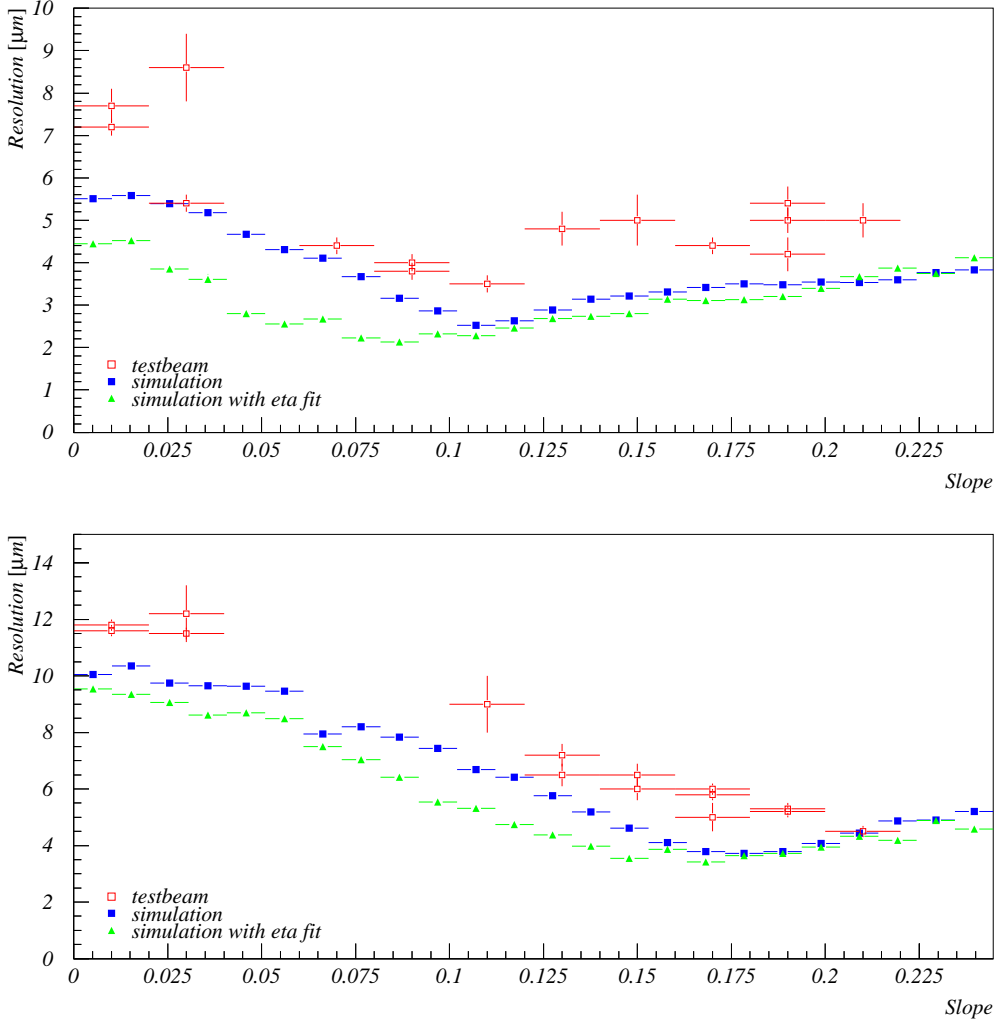
16

Figure 17: Resolution versus slope in VELO testbeam setup for $40~\mu$m (top) and $60~\mu$m strip pitches (bottom). The simulated resolution is compared to the measured residual. The expected resolution using an η-fit is shown for comparison (see Section 4.3).

inhomogeneous charge deposition when δ-rays are emitted (see section 2.3).

The dependence of the resolution on the energy cutoff T_{cut} was found to be very weak around the default value of $T_{\mathrm{cut}} = 20\,\mathrm{keV}$. At much higher cutoff values δ-ray emission is inhibited and the resolution becomes better. At $T_{\mathrm{cut}} = \mathcal{O}\,(1\,\mathrm{keV})$ the approximation of the δ-ray range is not valid anymore.

4.2.3 Charge sharing

Charge sharing has three distinct consequences on resolution:

1. It causes a dilution of the signal, reducing the S/N of the central strip and hence affects the efficiency in presence of high noise.

2. The sharing of the central strip signal with its neighbours decreases the probability of 1-strip clusters for perpendicular tracks, which can slightly increase the resolution.
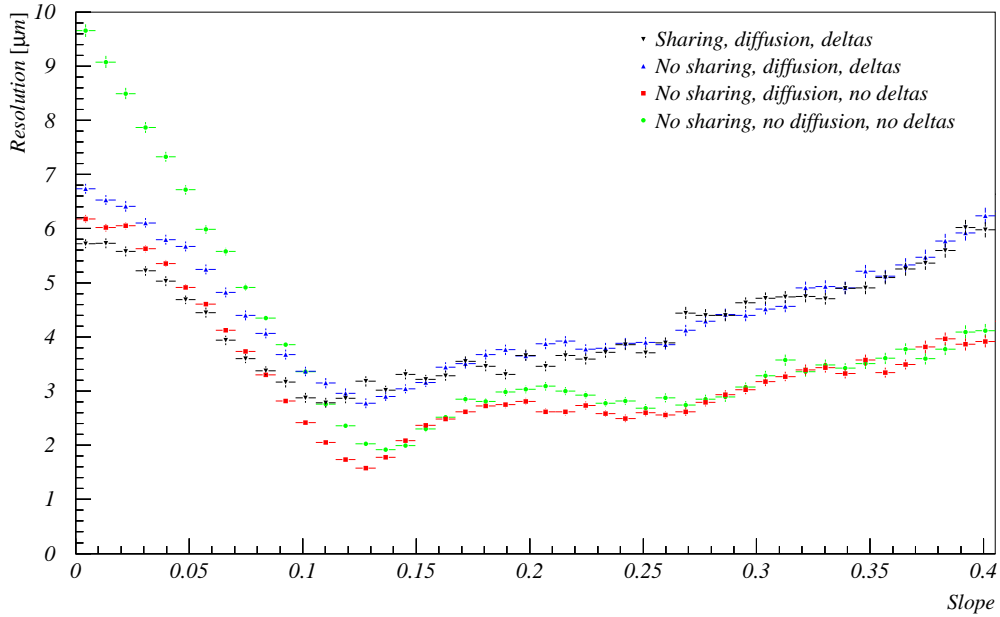
17

Figure 18: Resolution versus slope with various effects switched off. VELO testbeam settings are used with $40 \, \mu$m strips.
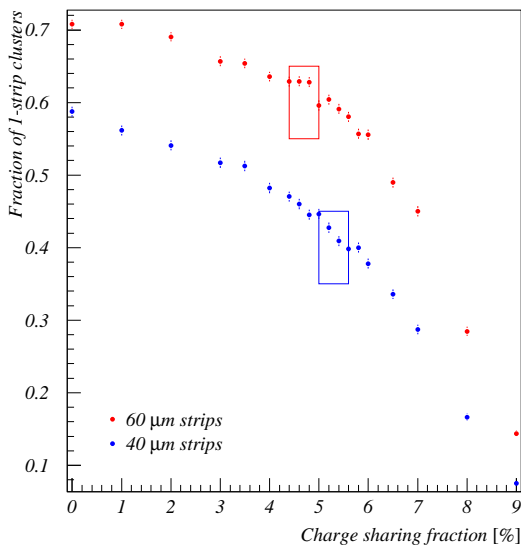

Figure 19: Fraction of 1-strip clusters versus charge sharing for in the VELO testbeam setup. The rectangles indicate the measurement at 1 standard deviation [1].
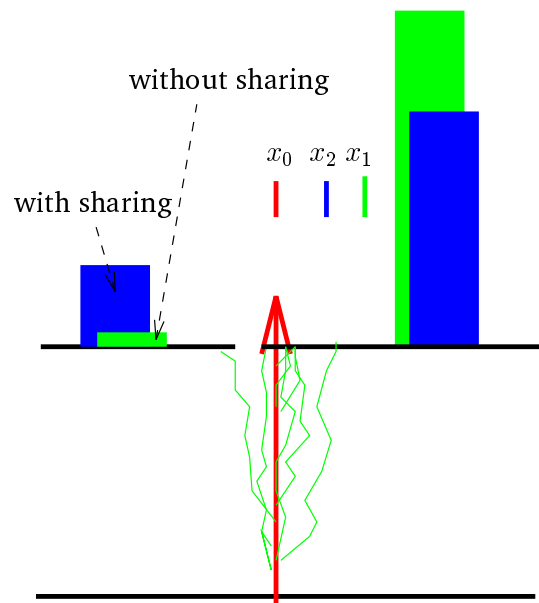

Figure 20: Effect of sharing on resolution of perpendicular tracks. See text.

The fraction of 1-strip clusters versus charge sharing is shown on Figure 19 and compared to the measured fractions and sharing.

3. Figure 20 shows how charge sharing corrects the center of mass position in the case

18

of two strip clusters: Perpendicular tracks that are ex-centered with respect to the center of the crossed strip i deposit the main part of the charge in strip and a small amount due to diffusion in the next (left) neighbouring strip $i - 1$. The center of mass of the resulting two-strip cluster is then very close to the center of strip i, which badly reflects the true position of the track. Charge sharing gives a small part of the charge in strip i to strip $i+1$, which corrects the "unfairness" of lateral diffusion. The non-linear behaviour of the charge fractions and hence of the reconstructed center-of-mass with the true entry point can be corrected by using an η-fit, as described in Section 4.3.

Adding up these contributions, the overall effect is positive for low angle tracks and becomes negligible at high angles.

4.2.4 A posteriori versus a priori mode

Because of the approximations made in the δ-ray generation (see Section 3.1.2) the average number of δ-rays is overestimated by 10% in the a posteriori mode and the inverse energy distribution of the δ-rays is cut off at low values (high energies). The net effect on the Landau shape, the resolution and the cluster sizes is negligible.

4.3 Resolution improvement using an η-fit

In all previous sections the resolution is computed comparing the center-of-mass of the cluster x_{CM} with the Monte Carlo true position x_{true} of the track in the middle of the silicon layer. This is a good approximation of the track position when its slope is not known. The distribution of $x_{\mathrm{CM}} - x_{\mathrm{true}}$ is shown in Figure 21 for almost perpendicular tracks. Introducing

$$\eta = \frac{\sum_{i=0}^{n-1} i C_i}{\sum_{i=0}^{n-1} C_i} \tag{22}$$

where S_i is the signal in strip $i = 0 \ldots n - 1$ of a n-strip cluster, one has

$$x_{\mathrm{CM}} = p\eta. \tag{23}$$

For 2-strip clusters η is

$$\eta = \frac{S_0}{S_0 + S_1}. \tag{24}$$

The x_{true} versus η-fit curve is shown in Figures 23 and 24 for two and three-strip clusters caused by almost perpendicular tracks. The definition of x_{CM} is equivalent to approximating this curve by a straight diagonal line. The distribution in Figure 21 reflects the difference between the true position and this approximation. A fit to this curve leads to a set of functions
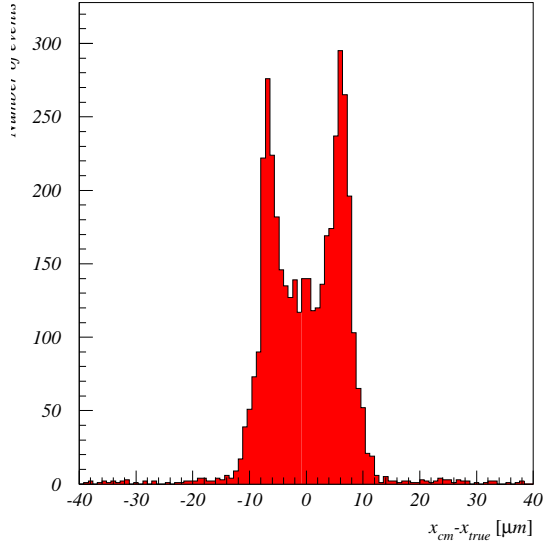
$$x_\eta = F_\alpha^{(p,n)}(\eta) \tag{25}$$

Figure 21: $x_{\mathrm{CM}} - x_{\mathrm{true}}$ distribution for perpendicular tracks.
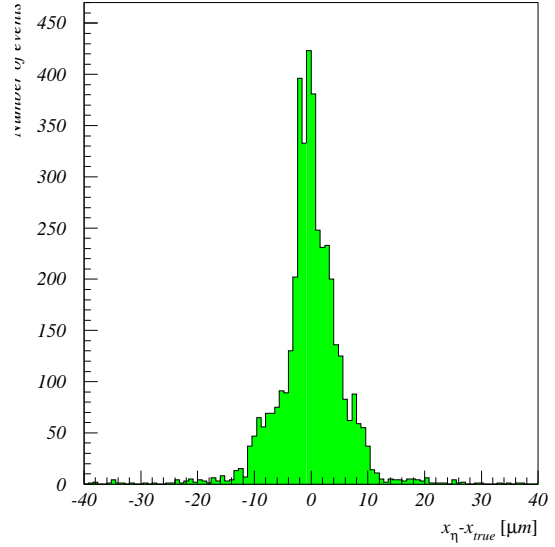

Figure 22: $x_\eta - x_{\mathrm{true}}$ distribution for perpendicular tracks.
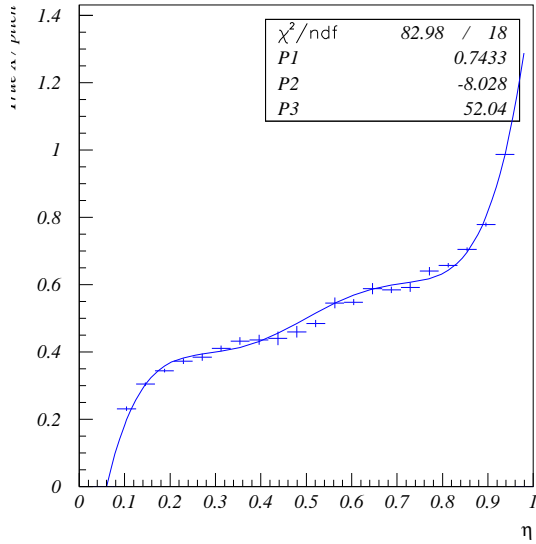

Figure 23: x_{true} versus η for 2-strip clusters. The best fit following (26) is shown for comparison.
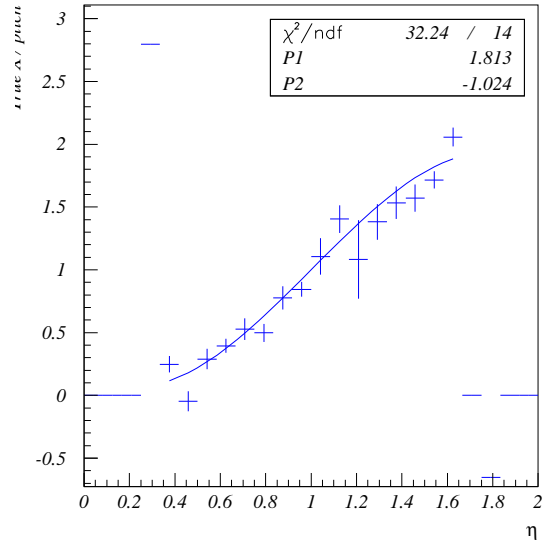

Figure 24: x_{true} versus η for 3-strip clusters. The best fit following (26) is shown for comparison.

at fixed slope α and pitch p. The curve is well described by a polynomial of the form

$$x_\eta = \frac{(n-1)p}{2} + a_\alpha^{(p,n)}\left(\eta - \frac{n-1}{2}\right) + b_\alpha^{(p,n)}\left(\eta - \frac{n-1}{2}\right)^3 + \ldots \qquad (26)$$

where the parameters $a_\alpha^{(p,n)}$ and $b_\alpha^{(p,n)}$ are to be determined by a fit to the simulated data.

For every cluster size and slope range we perform fits to polynomials of the order 3 and 5 and keep the fit with the lowest χ^2 per degree of freedom. In the case both χ^2 are too high, the fit is redone cutting off the extreme points of the distributions. If no convergence

20

is got the center of mass is used instead. In the case of Figure 23 a polynomial of 5th order is fit in the whole η range while in Figure 24 a polynomial of 3rd order is fit in the range 0.4–1.6.

The resulting residual distribution $x_\eta - x_{\text{true}}$ is shown in Figure 22 and the overall resolution versus the slope is shown on Figure 17. The η-fit increases the resolution by about $1\,\mu\text{m}$ for perpendicular tracks and the effect is non-negligible for slopes up to the optimal slope around 100 mrad. This procedure allows some correction of the bias introduced by charge sharing and diffusion but the resolution is still affected by δ-rays and noise.

This correction can only be done once the track is found and its slope known. For the first iteration in the pattern recognition algorithm x_{CM} has to be used.

4.4   Resolution in the VELO

The optimized VELO geometry differs from the testbeam setup by a lower thickness (220 versus 300 μm) and smaller pitches (down to 20 μm). The expected S/N ratio running at 40 MHz is in the range 10 to 20 rather than 50. The consequences are bigger clusters and a worse resolution (both because of noise). The expected resolutions are shown in Figures 25 for the optimized design and 26 for the baseline scenario.

At identical pitches, the resolution measured at testbeam is better because of the very high signal-to-noise ratio.

The clustering algorithm will be challenging in the optimized detector. In 20 μm-pitch strips only 50% of the total charge is deposited on average in the central strip. This fraction decreases with increasing angle. The S/N ratio of the central strip becomes thus about 8, causing inefficiencies and loss of resolution. This effect is visible on the resolution curve for angles above 200 mrad.

4.5   Analogue versus binary readout

The effect of analogue and binary readout on resolution has been studied for the Technical Proposal using a less developed version of the simulation [3]. We reproduce here the results for the TDR geometry and using the latest version of the simulation described.

In a binary readout scheme, the data would be zero-suppressed on the front-end chip and only a list of hit strips would be send to the ODE. Thus the granularity of the clustering would be of pitch/2. Figure 27 shows that the resolution is almost flat versus noise. Is is above the

A 2-bit and 4-bit digital readout scheme is also presented. In such a scheme, the data would be digitized on a dynamic range of 4 and 16 respectively. This improves the granularity to pitch/8 and pitch/32 respectively.

4.6   Resolution in the Inner Tracker

In the Inner Tracker a good resolution is only marginally important for physics but may be a good help to the pattern recognition for the high energy tracks where little multiple scattering is expected.

Figure 28 shows the expected resolution in a single silicon Inner Tracker layer. As most clusters are single-strip, the resolution is only marginally better than pitch/$\sqrt{12} = 68\,\mu\text{m}$ for low-angle tracks.
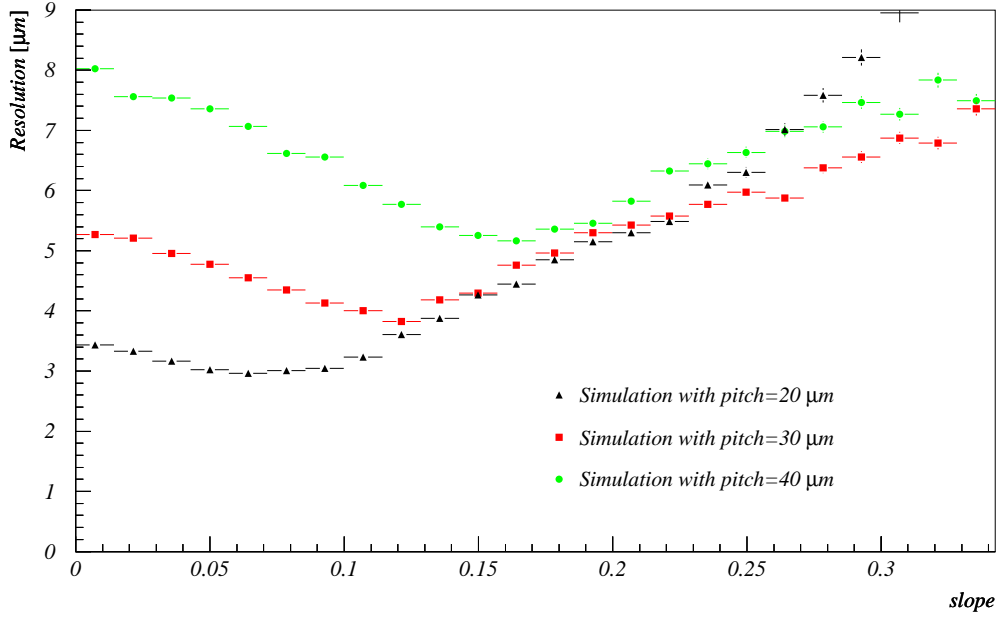
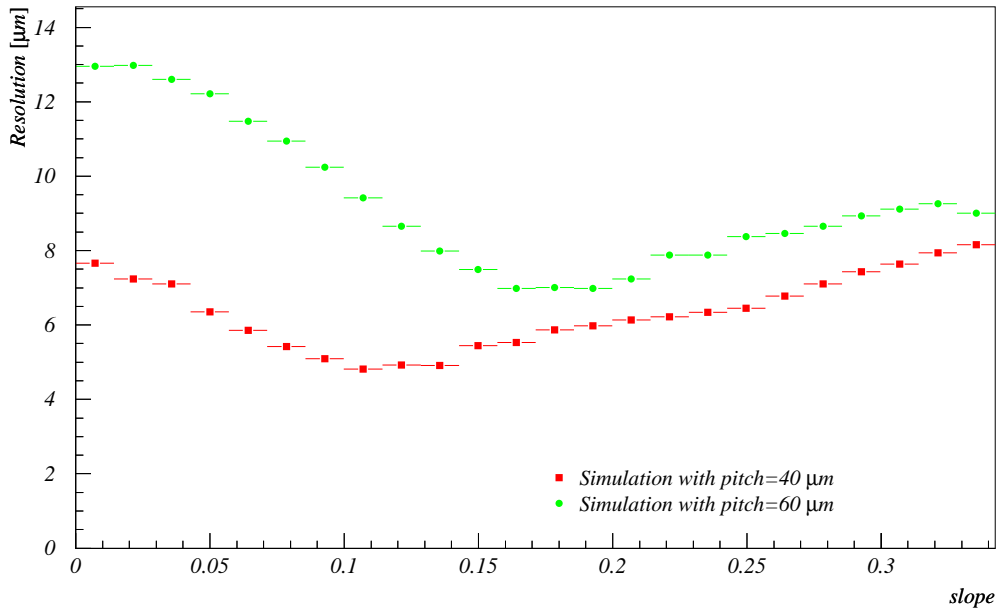Figure 25: Resolution versus slope in optimized VELO. The parameters are listed in Table 3 (page 14).

Figure 26: Resolution versus slope in VELO TDR baseline design. The parameters are listed in Table 3 (page 14).

A Expected number of δ-rays

In the a posteriori mode of the simulation, one would like to know the distribution $\mathcal{P}(N_\delta|E_\delta)$ of the number of δ-rays knowing their total energy E_δ. This can be solved
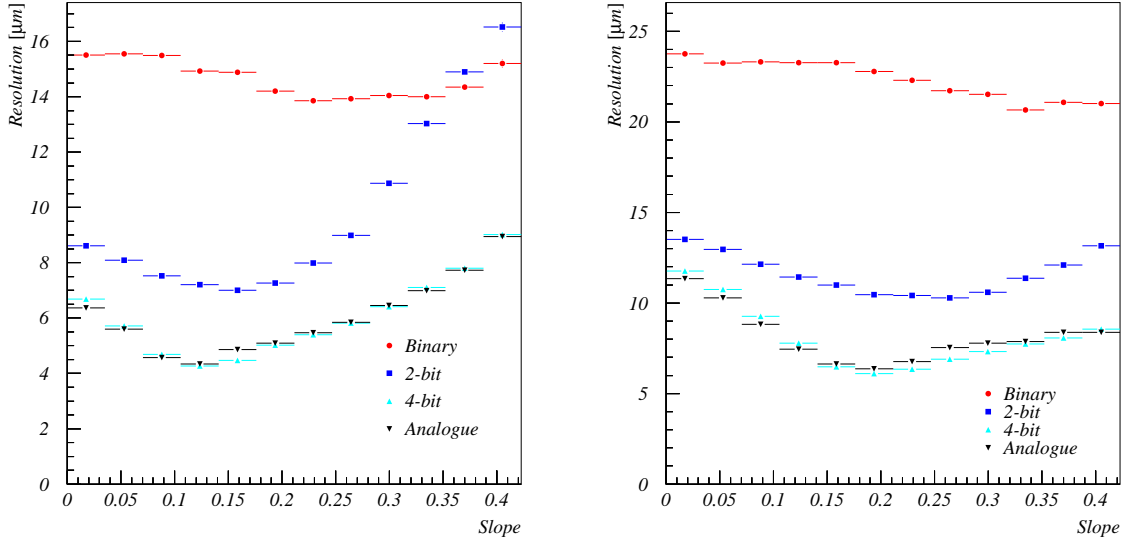
Figure 27: Resolution versus slope for analogue, binary, 2-bit and 4-bit readout. Left: 40 μm pitch, right: 60 μm pitch.
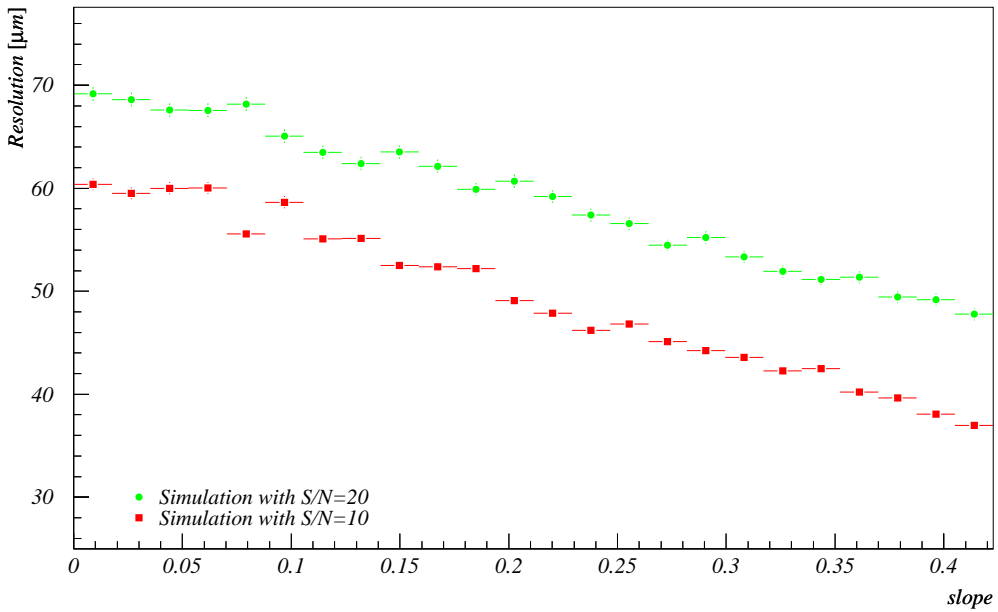

Figure 28: Resolution versus slope in the Inner Tracker with $S/N = 10$ and $S/N = 20$. The parameters are listed in Table 3 (page 14).

using Bayes' theorem

$$\mathcal{P}\left(N_\delta | E_\delta\right) = \frac{f_{N_\delta}(E_\delta)\mathcal{P}\left(N_\delta\right)}{f_\Sigma(E_\delta)} \tag{27}$$

23

where $f_{N_\delta}(E_\delta) = f(E_\delta|N_\delta)$ is the density of the total energy deposited by N_δ δ-rays. The distribution of the total energy E_δ given to δ-rays is

$$f_\Sigma(E_\delta) = \sum_{N_\delta=1}^{\infty} \mathcal{P}(N_\delta) f(E_\delta|N_\delta). \qquad (28)$$

These densities $f(E_\delta|N_\delta)$ follow from the probability density $f_1(T_\delta) = f(E_\delta|N_\delta=1)$ of the energy of one δ-ray (see section 2.2). The distribution $f_n(Z = X + Y) = f(Z|N_\delta=n)$ with $f_{n-1}(X) = f(X|N_\delta=n-1)$ and $f_1(Y) = f(Y|N_\delta=1)$ is

$$f_n(Z\!=\!z) = \int_{\max((n-1)T_{\mathrm{cut}}, z-T_{\mathrm{max}})}^{\min((n-1)T_{\mathrm{max}}, z-T_{\mathrm{cut}})} f_{n-1}(X\!=\!x) f_1(Y\!=\!z-x) \mathrm{d}x \qquad (29)$$

provided the densities $f_{n-1}(X)$ and $f_1(Y)$ are not correlated, which is not true when x or y becomes large and the particle looses a significant amount of its kinetic energy. In principle this correlation can be taken into account by updating T_{max} and β in $f_1(Y)$ accordingly.

   This direct procedure unfortunately leads to non-analytical expressions. The situation is easier to handle when the inverse energy distribution is used.

A.1   Inverse energy distribution of n δ-rays

The same procedure as described above is applied to the inverse energy distribution $u_\delta = 1/T_\delta$. The probability density function for this variable follows from (17)

$$f_1(u_\delta) = \begin{cases} 0 & u_\delta \leq u_{\mathrm{max}} \\ K_1\left(\frac{1}{\beta^2} - \frac{u_{\mathrm{max}}}{u_\delta}\right) \simeq K_1 & u_{\mathrm{max}} < u_\delta \leq u_{\mathrm{cut}} \\ 0 & u_{\mathrm{cut}} < u_\delta \end{cases} \qquad (30)$$

where $u_{\mathrm{cut}} = 1/T_{\mathrm{cut}}$, $u_{\mathrm{max}} = 1/T_{\mathrm{max}}$ and K_1 is a normalization constant

$$\int_0^\infty f_1(u_\delta) \mathrm{d}u_\delta = 1 \qquad \Rightarrow \qquad K_1 \simeq \frac{1}{u_{\mathrm{cut}}}$$

From this point the flat low-energy approximation $f_1(u_\delta) = 1/u_{\mathrm{cut}}$ for $u_{\mathrm{max}} < u_\delta \leq u_{\mathrm{cut}}$ is used.

   Two random variables X and Y representing the inverse total energies of any number of δ-rays do not add up but

$$\frac{1}{Z} = \frac{1}{X} + \frac{1}{Y} \qquad \Rightarrow \qquad Y = \frac{XZ}{X-Z}.$$

The distribution $f_n(Z\!=\!z)$ of the inverse energy of n δ-rays ($n \geq 2$) becomes

$$f_n(Z\!=\!z) = K_n \int_{\max\left(\frac{u_{\mathrm{max}}}{n-1}, \frac{z u_{\mathrm{cut}}}{u_{\mathrm{cut}}-z}\right)}^{\min\left(\frac{u_{\mathrm{cut}}}{n-1}, \frac{z u_{\mathrm{max}}}{u_{\mathrm{max}}-z}\right)} f_{n-1}(X\!=\!x) f_1\left(Y\!=\!\frac{zx}{x-z}\right) \mathrm{d}x \qquad (31)$$

24

where K_n is a normalization and the limits are defined by the validity ranges of the functions f_{n-1}

$$\frac{u_{\max}}{n-1} \le x \le \frac{u_{\mathrm{cut}}}{n-1}$$

and f_1

$$u_{\max} < y = \frac{zx}{x-z} \le u_{\mathrm{cut}} \qquad \Rightarrow \qquad \frac{zu_{\mathrm{cut}}}{u_{\mathrm{cut}}-z} \le x \le \frac{zu_{\max}}{u_{\max}-z}.$$

These limits define three ranges in z corresponding to three functions $f_n^{(i)}(z)$, $f_n^{(ii)}(z)$ and $f_n^{(iii)}(z)$

$$f_n^{(i)}(z) = K_n \int_{\frac{u_{\max}}{n-1}}^{\frac{zu_{\max}}{u_{\max}-z}} f_{n-1}(x)\,\mathrm{d}x \qquad \frac{u_{\max}}{n} < z \le \frac{u_{\mathrm{cut}}u_{\max}}{u_{\max}+(n-1)u_{\mathrm{cut}}}$$

$$f_n^{(ii)}(z) = K_n \int_{\frac{zu_{\mathrm{cut}}}{u_{\mathrm{cut}}-z}}^{\frac{zu_{\max}}{u_{\max}-z}} f_{n-1}(x)\,\mathrm{d}x \qquad \frac{u_{\mathrm{cut}}u_{\max}}{u_{\max}+(n-1)u_{\mathrm{cut}}} < z \le \frac{u_{\mathrm{cut}}u_{\max}}{(n-1)u_{\max}+u_{\mathrm{cut}}}$$

$$f_n^{(iii)}(z) = K_n \int_{\frac{zu_{\mathrm{cut}}}{u_{\mathrm{cut}}-z}}^{\frac{u_{\mathrm{cut}}}{n-1}} f_{n-1}(x)\,\mathrm{d}x \qquad \frac{u_{\mathrm{cut}}u_{\max}}{(n-1)u_{\max}+u_{\mathrm{cut}}} < z \le \frac{u_{\mathrm{cut}}}{n}$$

As $u_{\mathrm{cut}} \gg u_{\max}$, for a small number of δ-rays one has

$$\frac{u_{\mathrm{cut}}u_{\max}}{(n-1)u_{\max}+u_{\mathrm{cut}}} \simeq u_{\max},$$

and hence only the function $f_n^{(iii)}(z)$ is defined in the validity range of the low-energy approximation. Thus it is sensible to approximate the density function of n δ-rays by $f_n^{(iii)}(z)$. This function does not depend on $u_{\max}$.

Applying this procedure one gets the following functions $f_n(z)$ defined in the range $0 < z \le \frac{u_{\mathrm{cut}}}{n}$

$$f_1(z) = \frac{1}{u_{\mathrm{cut}}} \tag{32}$$

$$f_2(z) = \frac{u_{\mathrm{cut}}-2z}{u(u_{\mathrm{cut}}-z)(1-\log 2)} \tag{33}$$

$$f_3(z) = \frac{2\left(u_{\mathrm{cut}}-3z+(u_{\mathrm{cut}}-z)\log\frac{u_{\mathrm{cut}}-z}{2(u_{\mathrm{cut}}-2z)}\right)}{(2-\log\frac{27}{4})u_{\mathrm{cut}}(u_{\mathrm{cut}}-z)} \tag{34}$$

$$f_4(z) = \frac{1}{u_{\mathrm{cut}}}\frac{1}{2(u_{\mathrm{cut}}-z)}\left(2u_{\mathrm{cut}}-8z+(u_{\mathrm{cut}}-z)\log\left[\frac{u-z}{3(u_{\mathrm{cut}}-3z)}\right]\right. \tag{35}$$

$$\left.+2(u_{\mathrm{cut}}-z)\log\left[\frac{2(u_{\mathrm{cut}}-z)}{3(u_{\mathrm{cut}}-2z)}\right]-2z\log\left[\frac{u_{\mathrm{cut}}-2z}{2(u_{\mathrm{cut}}-3z)}\right]\right)$$

$$\cdots$$

The functions f_1 to f_3 are normalized. f_4 is not normalizable analytically. For $n > 4$ there is no analytical solution anymore. A numerical analysis shows that these function tend towards a linear shape when the average number of emitted δ-rays is small. In the simulation we use a linear approximation for $n \ge 3$

$$f_n(z) = \frac{2n}{u_{\mathrm{cut}}}\left(1-\frac{nz}{u_{\mathrm{cut}}}\right). \tag{36}$$

Acknowledgments

References

[1] PAOLO BARTALINI ET AL. VELO telescope resolution and efficiency measurements. LHCb VELO 2000-099, October 2000.

[2] VICTORIA WRIGHT ET AL. Study of Resolution of VELO Test-Beam Telescope. LHCb VELO 2000-103, November 2000.

[3] PATRICK KOPPENBURG. Comparison of analogue and binary read-out in the silicon strips vertex detector of LHCb. LHCb TRAC 97-020, 1997.

[4] LHCb, ANDREI TSAREGORODTSEV. SICB user guide, GEANT3-based simulation package for the LHCb experiment, June 1997.

[5] DAVID STEELE. The R-φ silicon vertex detector simulation as implemented in SICB. LHCb TRAC 98-004, 1998.

[6] CERN. GEANT— Detector description and Simulation Tool. CERN Program Library Long Writeup W5013.

[7] D.E. GROOM ET AL. Review of Particle Physics. *The European Physical Journal*, C(15), 2000.

[8] R.M. STERNHEIMER. The Density Effect for the Ionization Loss in Various Materials. *Physical Review*, 88:851–859, 1952.

[9] BRUNO ROSSI. *High-Energy Particles*. Prentice-Hall, 1952.

[10] H. BETHE. Zur Theorie des Durchgangs schneller Korpuskularkörper durch Materie. *Annalen Phys.*, 5:325–400, 1930.

[11] ANNA PEISERT. Silicon Microstrip Detectors. In FABIO SAULI, editor, *Instrumentation in High Energy Physics*, volume 9 of *Advanced Series on Directions in High Energy Physics*, pages 1–81. World Scientific, 1993.

[12] G. HALL. Ionization Energy Losses of Highly Relativistic Charged Particles in Thin Silicon Layers. *Nucl. Instr. Meth.*, A220:356–362, 1984.

[13] P.V. VAVILOV. Ionization losses of high energy heavy particles. *Soviet Physics JETP*, 5:749, 1957.

[14] M.J. BERGER. Stopping-Power and Range Tables for Electrons, Protons, and Helium Ions. http://physics.nist.gov/PhysRefData/Star/Text/contents.html.

[15] Y. ASANO ET AL. Monte Carlo Simulations of Effects due to Delta Rays in Aluminum Drift Tube Counters. *Nucl. Instrum. Meth.*, A259:438, 1987.

[16] G.Z. MOLIÈRE. Theorie der Streuung schneller geladener Teilchen: Einzelstreuung am abgeschmierten Coulomb-Feld. *Z. Naturforsch.*, 2:133, 1947.

[17] G.Z. MOLIÈRE. Theorie der Streuung schneller geladener Teilchen: Mehrfach- und Vielfachstreuung. *Z. Naturforsch.*, 3:78, 1947.

[18] SIMON RAMO. Currents induced by electron motion. *Proc. IRE*, 27:584, 1939.

[19] HEINZ PERNEGGER. *The Silicon Ministrip Detector of the Delphi Very Forward Tracker.* Dissertation ausgeführt zum Zweck der Erlangung des akademischen Grades eines Doktors der technischen Wissenschaften, Technische Universität Wien, February 1996.

[20] THEMIS BOWCOCK ET AL. VELO geometry optimisation. LHCb VELO 2000-090, October 2000.

[21] LHCb, P.R. BARBOSA MARINHO ET AL. *LHCb* VELO *Technical Design Report.* CERN, Genève, 2001. CERN/LHCC/2001-0011.

[22] OLAF STEINKAMP. A Possible Layout of an Inner Tracker Silicon Detector. LHCb IT 2000-109, December 2000.

[23] STEFANIA SALADINO. *Study of Vertex Silicon Detector For LHC Experiments.* Dottorato di Ricerca in Fisica, Università degli Studi di Bari, 1999.